CrossMark

RESEARCH ARTICLE

DCE-MRI of hepatocellular carcinoma: perfusion quantification with Tofts model versus shutter-speed model—initial experience

Guido H. Jajamovich[1] · Wei Huang[2] · Cecilia Besa[1] · Xin Li[2] · Aneela Afzal[2] · Hadrien A. Dyvorne[1] · Bachir Taouli[1]

Abstract

Objective To quantify hepatocellular carcinoma (HCC) perfusion and flow with the fast exchange regime-allowed Shutter-Speed model (SSM) compared to the Tofts model (TM).

Materials and methods In this prospective study, 25 patients with HCC underwent DCE-MRI. ROIs were placed in liver parenchyma, portal vein, aorta and HCC lesions. Signal intensities were analyzed employing dual-input TM and SSM models. ART (arterial fraction), K^{trans} (contrast agent transfer rate constant from plasma to extravascular extracellular space), v_e (extravascular extracellular volume fraction), k_{ep} (contrast agent intravasation rate constant), and τ_i (mean intracellular water molecule lifetime) were compared between liver parenchyma and HCC, and ART, K^{trans}, v_e and k_{ep} were compared between models using Wilcoxon tests and limits of agreement. Test–retest reproducibility was assessed in 10 patients.

Results ART and v_e obtained with TM; ART, v_e, k_{e} and τ_i obtained with SSM were significantly different between liver parenchyma and HCC ($p < 0.04$). Parameters showed variable reproducibility (CV range 14.7–66.5 % for both models). Liver K^{trans} and v_e; HCC v_e and k_{ep} were significantly different when estimated with the two models ($p < 0.03$).

Conclusion Our results show differences when computed between the TM and the SSM. However, these differences are smaller than parameter reproducibilities and may be of limited clinical significance.

Keywords MRI · Hepatocellular carcinoma · Liver

Introduction

Hepatocellular carcinoma (HCC) is the third leading cause of cancer-related death worldwide [1], and its incidence is increasing in the United States [2]. The growth and progression of histological malignancy of HCC are associated with the formation of new blood vessels [3] which happens through angiogenesis and/or by recruiting proangiogenic bone marrow-derived cells [4]. This capability of sustained angiogenesis is one of the hallmarks of cancer [5, 6]. In order to characterize HCC, the quantification of vascular characteristics of HCC is important. MRI and CT play an important role in HCC diagnosis, staging, and treatment planning [7–13].

Dynamic contrast-enhanced (DCE)-MRI is a non-invasive methodology that allows tissue perfusion quantification. Generally, DCE-MRI consists of acquisition of T1-weighted MR images before, during and after an IV injection of a gadolinium-based contrast agent (CA) and the perfusion quantification is the result of modeling the tracer pharmacokinetics as it distributes through the tissue of interest [14–16]. One of such pharmacokinetic models was introduced by Tofts and Kermode [26–28] (TM: Tofts model). This model has been used to extract vascular permeability characteristics of HCC and to assess response to treatment [18, 22, 23, 29]. The TM has also been modified to allow two inputs in order to estimate liver parenchyma perfusion parameters as the liver has both arterial and venous inputs. The resulting dual input TM is equivalent

✉ Bachir Taouli
bachir.taouli@mountsinai.org

[1] Department of Radiology and Translational and Molecular Imaging Institute, Icahn School of Medicine at Mount Sinai, 1470 Madison Avenue, New York, NY 10029, USA

[2] Oregon Health & Science University, Portland, OR, USA

to the dual-input single compartment model proposed by Materne et al. [19, 20], which had been validated in vivo in an animal model [30] and used for liver fibrosis detection [31–34].

Currently, there is no consensus regarding the pharmacokinetic model that should be used to quantify HCC perfusion parameters [17]. For example, Taouli et al. [18] utilized a dual-input single compartment model, while Sahani et al. [21] used a hybrid model composed of a distributed and compartmental component for the intravascular and extravascular spaces, respectively, to extract perfusion parameters from dynamic CT. Due to the fact that HCC lesions receive their supply mainly from the hepatic artery, single input models have also been used by some investigators [17, 22, 23]. Jarnagin et al. [24] and Yopp et al. [25] used the dual compartment version of the TM to quantify changes after therapy. All these studies have used different analysis methods, showing that the post-processing of HCC and liver perfusion data is not standardized and making comparisons between studies difficult.

The TM has similarities with well-established kinetic models used in nuclear medicine where the tracer is measured directly. However, when used in MRI, the CA is measured indirectly through observing its effect on tissue ^1H_2O longitudinal relaxation rate constant, R_1 [35]. The TM is essentially derived from the tracer kinetic model with the assumption of linear relationship between CA concentration and R_1, equivalent to assuming infinitely fast intercompartmental equilibrium water exchange kinetics [35]. However, this assumption might not hold true when there is significant CA extravasation during CA bolus passage through the tissue of interest [35].

The Shutter-Speed family of DCE-MRI pharmacokinetic models takes into consideration the finite tissue intercompartmental equilibrium water exchange kinetics [35–47], which can include both transcytolemmal and transendothelial water exchanges. However, the more compartments are taken into account, the more variables need to be included for data modeling [43]. The fast exchange regime (FXR)-allowed Shutter-Speed model (SSM) version is a two-site-exchange model accounting for transcytolemmal water exchange. The FXR introduces only one parameter in addition to the conventional parameters of the TM: the mean intracellular water molecule lifetime, τ_i. This version of the SSM has been used to quantify perfusion of breast [48] and prostate cancer [49], but not in the liver. It has been suggested that τ_i may reflect cellular metabolic activity [50, 51].

Given that the SSM presumably models the underlying MRI physics more realistically than the TM and that the SSM-unique τ_i parameter has the potential to provide metabolic information of HCC, the objective of this initial study was to perform quantitative pharmacokinetic analysis of DCE-MRI data from HCC and non tumorous liver parenchyma using the TM and the FXR SSM version, both adapted to allow for two vascular inputs. In addition, the test–retest reproducibility of DCE-MRI parameters was assessed for both models. A secondary objective was to assess the relationship of HCC perfusion parameters with histopathologic markers.

Materials and methods

Subjects

This HIPAA compliant prospective study was funded by the National Cancer Institute (Grant Numbers U01 CA172320 and U01 CA154602), and approved by the Icahn School of Medicine at Mount Sinai Program for the Protection of Human Subjects. Written consent was obtained from all patients prior to the exam. The study included 25 consecutive patients with chronic liver disease and HCC that underwent a DCE-MRI exam at Mount Sinai Hospital. Patients were enrolled from June 2013 to June 2014. Liver diseases were related to the following etiologies: chronic hepatitis C ($n = 18$), chronic hepatitis B ($n = 5$), nonalcoholic steatohepatitis ($n = 1$), and unknown cause ($n = 1$).

10 patients were scanned twice for assessment of test–retest parameter reproducibility with a mean interval of 5 ± 3 days (range 2–11 days) between the two scans (and no interval therapy).

Patients with severe renal dysfunction [estimated glomerular filtration rate (eGFR) <30 ml/min/1.73 m^2] were excluded from the study in order to minimize the risk of nephrogenic systemic fibrosis [52]. Since portal venous flow can increase postprandially [53], all subjects were asked to fast for 6 h before the MRI study.

MRI acquisition

Examinations were performed with one of three state-of-the art MRI systems (1.5T Siemens Aera, 3T Siemens Skyra, and 3T Siemens mMR, Erlangen, Germany), each equipped with a multichannel spine and body matrix coil for RF receiving. One patient underwent both examinations in the 3T Siemens Skyra system, 6 patients in the 1.5T Siemens Aera system, and 3 patients had their first exams in the 1.5T Aera System and the second ones in the 3T Siemens mMR system.

Patients were positioned arms up in supine position. In addition to routine clinical sequences used to localize and characterize the liver and liver lesions, the following sequences were acquired:

Table 1 DCE-MRI pulse sequence parameters

Scanner	1.5T[a] (n = 26)	3.0T[b] (n = 6)	3.0T[c] (n = 3)
Sequence type	3D GRE (FLASH)	3D GRE (FLASH)	3D GRE (FLASH)
Orientation	Axial	Axial	Axial
Repetition time (ms)	2.74	2.69	2.71
Echo time (ms)	1.09	0.98	0.98
Flip Angle	11.5	11.5	11
Field of view (mm^2)	370 × 250	370 × 260–280	400 × 300
Acquisition matrix	192 × 106	192 × 107	192 × 115
Slice thickness (mm)	4	4	4.5
Number of slices	44	44	44
Acceleration[d]	R = 3	R = 2	R = 2
Acquisition time	202.4 ± 0.4 s	246.4 ± 50.3	361

[a] Siemens Aera; [b] Siemens Skyra; [c] Siemens mMR

GRE: gradient echo, [d] using CAIPIRINHA: Controlled Aliasing in Parallel Imaging Results in Higher Acceleration

- Breath-hold axial, coronal and sagittal T2-weighted HASTE sequences to localize the abdominal aorta, portal vein, liver, and HCC tumors.
- T1 mapping: The baseline hepatic T1 value was obtained using a breath-hold Look-Locker sequence [54] before the CA injection during DCE-MRI.
- DCE-MRI of the liver (Table 1): a 3D-FLASH sequence was used in the axial plane to obtain acquisitions before, during and after the injection of a CA bolus at a dose of 0.05 mmol/Kg (gadobenate dimeglumine, Multihance, Bracco) injected at 3 mL/s followed by a 25 mL saline flush using an MR-compatible power injector. The 3D acquisition allowed us to cover the entire liver. 100 time points were acquired with an average temporal resolution of 2.3 ± 0.2 s (range 2.0–3.6 s) and a total acquisition time of ~4 min. Patients were allowed to breath freely.

Image analysis

Images were processed by observer 1 (GHJ, postdoctoral fellow with 3 years of experience in MR image analysis) supervised by a body MR radiologist (observer 2, BT) with 10 years' experience. HCC lesions were identified in consensus fashion by observers 2 and 3 (CB, a radiologist with 4 years' experience in Body MRI) based on routine sequences including contrast-enhanced T1-weighted images and images taken after the injection of CA. Regions of interest (ROIs) were placed to measure signal intensity

(SI) in the abdominal aorta at the level of the celiac axis, the portal vein at the level of the porta hepatis, liver parenchyma and HCC lesions after image coregistration with in-house software implemented in MatLab 2014a (MathWorks, Natick, MA) (Fig. 1). ROIs were placed at one time point and automatically copied to all available DCE time points. Manual correction was used when the copied ROI did not cover the area of interest. The abdominal aorta was used as a surrogate of the hepatic artery as the small size of the latter prevented an accurate measurement. For untreated HCCs, ROIs encompassed the whole lesion in the axial view where the lesion was greater; for treated/partially necrotic lesions, ROIs were placed only in the viable component (identified by observer 3 on contrast-enhanced images). For each patient, only the largest HCC lesion was analyzed as the processing of the lesions is more robust with largest lesions.

Pharmacokinetic modeling

The mean SI in each ROI was used for pharmacokinetic analysis. The conversion from SI to contrast agent relaxation rate constant was performed by inverting the nonlinear relationship given by the SPGR signal equation as described in [54, 55]. The CA is delivered to the liver and the HCC through both the hepatic artery and the portal vein. The two inputs can be added in order to construct a single input with an unknown arterial fraction (ART, %) that needs to be estimated jointly with the perfusion parameters. Specifically, let $R_{AIF}(t)$ and $R_{VIF}(t)$ be the relaxation rate constants observed in the arterial and venous input functions, then we define the relaxation rate constant of the input, $R_I(t)$, as follows.

$$R_I(t) = \frac{ART}{100} R_{AIF}(t) + \left(1 - \frac{ART}{100}\right) R_{VIF}(t - \tau_{VIF}), \quad (1)$$

where $0 \leq ART \leq 100$ and τ_{VIF} is a relative delay between the arterial and venous input functions.

Once this equivalent single input was defined, we converted the relaxation rate constant to CA concentration $C_I(t)$ assuming linearity, as water exchange across blood cell membrane remains in the fast-exchange-limit condition [35, 36]. The relaxivity of the CA and pre-contrast blood T1 values were obtained from literature ([56, 57], respectively), with values of 8.1 L mmol^{-1} s^{-1} and 1480 ms for the 1.5 T system and 6.3 L mmol^{-1} s^{-1} and 1649 ms for the 3T system. Blood CA concentrations were converted to plasma concentrations using an assumed hematocrit value of 0.45 [58]. The pre-contrast T1 values for the liver parenchyma and HCC lesions were obtained from the T1 map. Then, we made use of the Tofts model for kinetic modeling of DCE-MRI data, given by
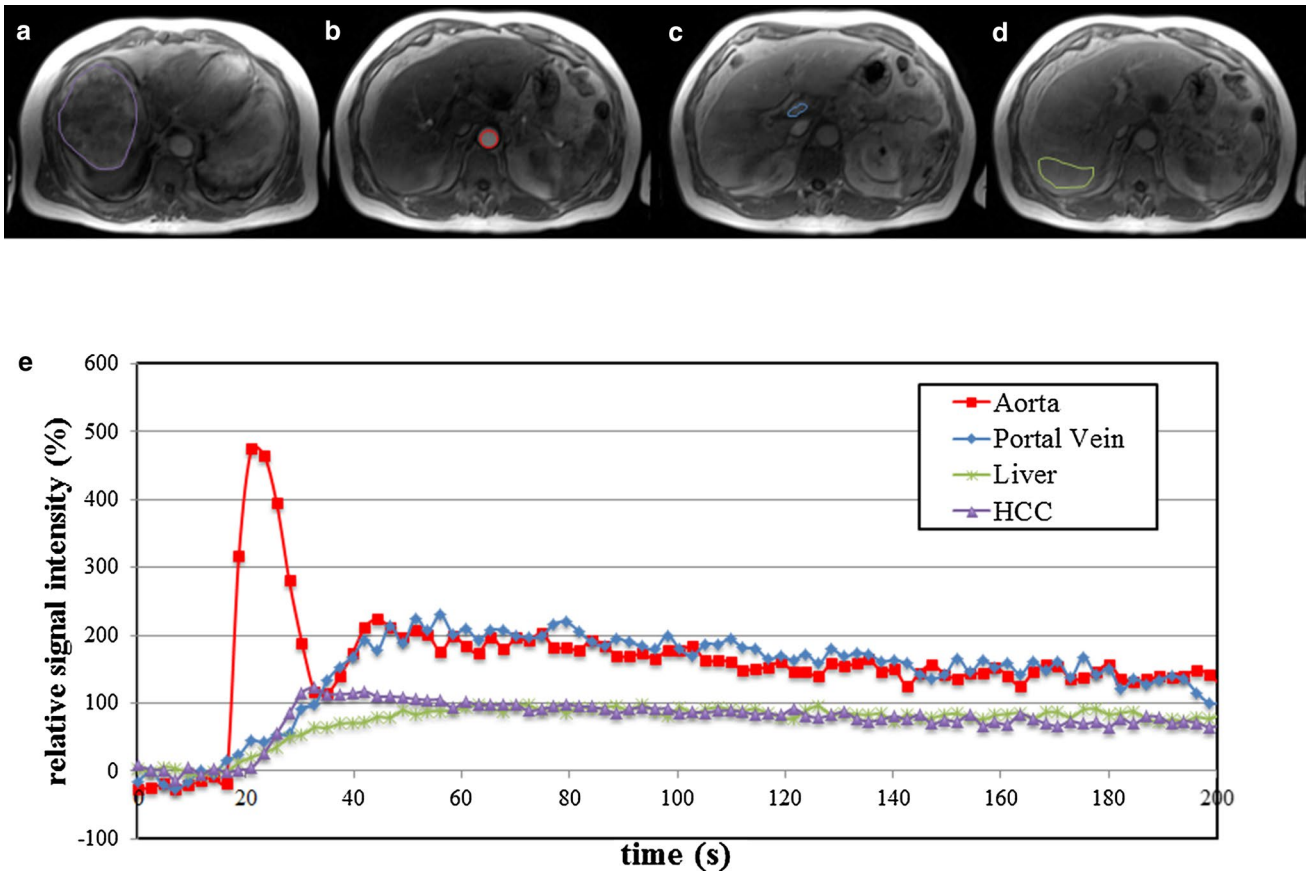
Fig. 1 66 year old male patient with large HCC in the right hepatic lobe (13 cm). Axial DCE-MR images acquired using 3D-FLASH sequence at 1.5T (TR/TE/FA 2.74/1.09/11.5°, matrix 192 × 106, slice thickness 4 mm, acceleration factor 3, 44 slices, 100 time points with temporal resolution of 2.02 s) demonstrate ROI placement in different regions at different time points: tumor (*purple*) acquired at 20 s post injection (**a**), abdominal aorta (*red*) (**b**, 11 s post injection), main portal vein (*blue*) (**c**, 28 s post injection), and liver parenchyma (*green*) (**d**, 55 s post injection). Plots below **e** demonstrate relative signal intensity versus time curve [y axis: $100 \times (\text{SI}/\text{SI}_0 - 1)$, with SI and SI_0 representing the signal intensity and signal intensity before enhancement, respectively]. Plot shows fast enhancement and subsequent washout of HCC as opposed to slow enhancement of liver parenchyma

$$C_{\text{tissue}}(t) = K^{\text{trans}} \int_0^t C_I(t' - \tau_{IN}) e^{-\frac{K^{\text{trans}}}{v_e}(t-t')} dt' \tag{2}$$

where $C_{\text{tissue}}(t)$ is the concentration curve observed in the tissue of interest, K^{trans} and v_e are the CA transfer rate constant from the blood plasma into the extravascular and extracellular space (EES) and the EES volume fraction, respectively, and τ_{IN} is the relative delay between the equivalent single input and $C_{\text{tissue}}(t)$. The CA intravasation rate constant, k_{ep}, can be calculated as K^{trans}/v_e. The effects of transcytolemmal water exchange are ignored in the TM, and thus $C_{\text{tissue}}(t)$ was converted from tissue $R_1(t)$ through a linear relationship:

$$R_1(t) = R_{10} + r_1 C_{\text{tissue}}(t), \tag{3}$$

where R_{10} is the pre-contrast tissue R_1 (measured through T1 mapping) and r_1 is the CA relaxivity.

We also used the SSM model to fit the DCE-MRI data, given by

$$R_1(t) = \frac{1}{2}\left[\left\{2R_{1i} + \frac{r_1 K^{\text{trans}}}{v_e}\int_0^t C_I(t' - \tau_{IN})e^{-\frac{K^{\text{trans}}}{v_e}(t-t')}dt' \right. \right.$$
$$\left. + \frac{R_{10} - R_{1i} + \frac{1}{\tau_i}}{v_e}\right\}$$
$$- \left\{\left[\frac{2}{\tau_i} + \frac{R_{1i} - R_{10} - \frac{1}{\tau_i}}{v_e} - \frac{r_1 K^{\text{trans}}}{v_e}\int_0^t C_I(t' - \tau_{IN})e^{-\frac{K^{\text{trans}}}{v_e}(t-t')}dt'\right]^2 \right.$$
$$\left. \left. + \frac{4(1 - v_e)}{\tau_i^2 v_e}\right\}^{1/2}\right] \tag{4}$$

where R_{1i} is the intracellular longitudinal relaxation rate constant [59] and was set to be equal to R_{10} [43]. In addition to the parameters present in the TM (K^{trans}, v_e and $k_{\text{ep}} = K^{\text{trans}}/v_e$), the SSM also returns the τ_i parameter. Note

Table 2 Coefficients of variation (mean and range %) and Bland–Altman limits of agreement (BALA %) for DCE-MRI parameters obtained with the Tofts model (TM) and the shutter-speed model (SSM) in the test–retest study ($n = 10$)

Parameter	Model	Liver	HCC
ART	TM		
	CV (%)	63.3 (4.9–137.2)	31.4 (0.0–138.6)
	BALA (%)	−267.6, 185.1	−152.9, 155.6
	SSM		
	CV (%)	66.5 (8.5–141.4)	54.9 (0.0–141.4)
	BALA (%)	−273.4, 185.2	−229.5, 198.1
K^{trans}	TM		
	CV (%)	47.1 (0.0–112.9)	28.9 (0.0–82.9)
	BALA (%)	−136.1, 174.8	−105.7, 134.8
	SSM		
	CV (%)	46.5 (0.1–113.5)	25.1 (0.0–94.9)
	BALA (%)	−144.4, 175.2	−119.2, 126.5
v_e	TM		
	CV (%)	37.9 (0.4–79.5)	36.3 (0.0–89.4)
	BALA (%)	−86.3, 139.9	−98.0, 158.9
	SSM		
	CV (%)	39.4 (1.5–74.1)	50.8 (2.0–93.1)
	BALA (%)	−89.1, 143.6	−106.2, 191.9
k_{ep}	TM		
	CV (%)	34.4 (3.2–87.9)	44.1 (3.3–82.9)
	BALA (%)	−128.9, 124.3	−160.3, 123.4
	SSM		
	CV (%)	32.2 (2.2–88.2)	38.2 (2.2–65.2)
	BALA (%)	−130.6, 117.5	−132.6, 47.3
τ_i	SSM		
	CV (%)	14.7 (0.0–55.9)	42.6 (0.0 − 130.5)
	BALA (%)	−69.4, 81.6	−206.1, 161.5

ART arterial fraction (%), K^{trans} CA transfer rate constant from the blood plasma into the extravascular and extracellular space (min^{-1}), v_e extravascular and extracellular space volume fraction, k_{ep} CA intravasation rate constant (min^{-1}), τ_i: mean intracellular water molecule lifetime (s)

Table 3 Estimated liver and HCC perfusion parameters (mean ± SD) using Tofts model (TM) and shutter-speed model (SSM) in 25 patients with 25 HCCs

Parameter	Model	Liver	HCC	p*
ART	TM	40.12 ± 26.75	85.12 ± 21.71	**<0.001**
	SSM	42.36 ± 27.17	77.44 ± 25.78	**<0.001**
	*p***	0.08	0.07	
	CV	12.5 (0.0–64.3)	11.7 (0.0–68.1)	
	BALA	−39.9, 55.7	−66.5, 43.8	
K^{trans}	TM	1.21 ± 0.63	1.34 ± 0.96	0.59
	SSM	1.05 ± 0.58	1.39 ± 1.09	0.26
	*p***	**<0.001**	0.39	
	CV	10.12 (0.1–39.0)	10.4 (0.0–31.2)	
	BALA	−41.2, 12,9	−40.5, 34.3	
v_e	TM	0.44 ± 0.14	0.37 ± 0.21	**0.02**
	SSM	0.40 ± 0.13	0.30 ± 0.12	**0.004**
	*p***	**<0.001**	**<0.001**	
	CV	6.9 (0.3–11.2)	14.5 (3.0–79.4)	
	BALA	−15.8, −3.8	−71.5, 34.7	
k_{ep}	TM	2.92 ± 1.59	4.25 ± 4.11	0.13
	SSM	2.75 ± 1.48	4.88 ± 4.60	**0.04**
	*p***	0.16	**0.03**	
	CV	5.3 (0.0–28.5)	13.7 (0.0–92.7)	
	BALA	−28.3, 19.5	−50.0, 79.6	
τ_i	SSM	0.11 ± 0.02	0.29 ± 0.53	**0.008**

Coefficients of variation (mean and range %) and Bland–Altman limits of agreement (BALA %) obtained for DCE-MRI parameters obtained with both models

ART arterial fraction (%), K^{trans} CA transfer rate constant from the blood plasma into the extravascular and extracellular space (min^{-1}), v_e extravascular and extracellular space volume fraction, k_{ep} CA intravasation rate constant (min^{-1}), τ_i: mean intracellular water molecule lifetime (s)

* *p* value computed using a Wilcoxon test when comparing a parameter in the liver parenchyma versus HCC; ** *p* value computed using a Wilcoxon test when comparing a parameter common to the TM and the SSM in a given tissue

that for the SSM, we do not need to convert relaxation rate constant time-course to concentration curves, avoiding the use of the linearity assumption.

Statistical analysis

Estimated perfusion parameters obtained with both the TM and SSM (i.e., ART, K^{trans}, v_e, and k_{ep}) in HCC tumors and liver were compared using Wilcoxon tests and by determining the Bland–Altman limits of agreement (BALA). The BALA quantifies the agreement by computing the differences for each parameter as estimated with the TM and SSM and by providing the corresponding 95 % confidence intervals [60]. Estimated perfusion parameters were also compared between HCC tumors and liver parenchyma using Wilcoxon tests. Test–retest reproducibility was assessed in 10 patients by computing the coefficient of variation (CV) and BALA. Finally, tumor perfusion parameters were compared between different tumor grades and between tumors with and without microvascular invasion using a Mann–Whitney *U* test. The statistical analysis was performed in MatLab 2014a (MathWorks, Natick, MA).

Results

25 HCC lesions were assessed (mean size 4.3 cm, range 1.4–14.0 cm) in 25 patients. One patient was treated with transcatheter arterial chemoembolization prior to MRI and presented with a partially necrotic HCC (approximately 30 % necrosis).

Fig. 2 Bland–Altman plots show the comparison of HCC perfusion parameters obtained with Tofts and Shutter-Speed models (differences were normalized by average parameter values). Resulting Bland–Altman limits of agreement (*red dash line*) are smaller than Bland-Altman limits of agreement for test–retest variability (see also Tables 2 and 3)
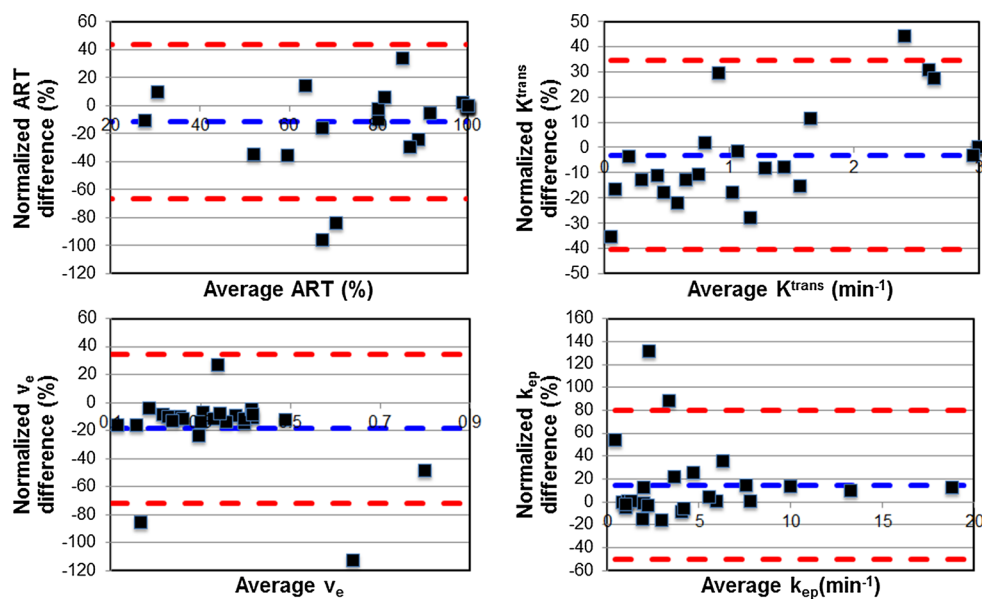
Histopathologic diagnosis of HCC was available in 15 patients after tumor resection performed an average of 11.5 days (range 4–23 days) after MRI scan. Tumors had the following grade distribution: moderately differentiated ($n = 11$) or poorly differentiated ($n = 4$). 11/15 HCC tumors demonstrated microvascular invasion.

Reproducibility of estimated perfusion parameters

Perfusion parameters showed variable reproducibilities for both TM and SSM analyses, with CV in the range of 14.7–66.5 %, depending on the parameter (Table 2). In HCC, ART and v_e estimated with the TM showed better reproducibilities than their SSM counterparts, while K^{trans} and k_{ep} showed better reproducibilities for the SSM. K^{trans} estimated with the SSM was the most reproducible parameter in HCC. Similar CV values were seen for all liver parameters of both models. Hepatic τ_i was the perfusion parameter with the best reproducibility and the best BALA.

Estimated perfusion parameters using the TM and the SSM

HCC parameters v_e and k_{ep} for the TM were significantly greater and lower, respectively, when compared to HCC parameters v_e and k_{ep} for the SSM ($p < 0.03$) (Table 3; Fig. 2). For these parameters, BALAs between models were smaller than the test–retest BALA for both the TM and the SSM, suggesting that the model differences are of limited clinical significance. ART and K^{trans} for the TM were not significantly different when compared to their SSM counterparts.

Liver K^{trans} and v_e were significantly higher for the TM when compared to their SSM counterparts ($p < 0.001$).

However, the two models displayed good agreement when estimating these two parameters in the liver, as determined by BALA [K^{trans} and v_e had BA limits of agreement of (-41.2, 12.9 %) and (-15.8, -3.8 %), respectively]. These two facts imply a significant but small bias. However, the limits of agreement were smaller than the test–retest parameter BALA (Table 2) for both models and therefore, the observed model differences in the parameters were also assumed to be of limited clinical importance. ART and k_{ep} measured in liver were not significantly different when estimated with the two models.

Comparison between HCC and liver parenchyma

Both the TM and SSM produced parameters with significant differences in HCC when compared to background liver (Table 3). ART was significantly higher while v_e was significantly lower in HCC tumors compared to liver parenchyma for both models ($p < 0.001$ and $p < 0.02$, respectively). k_{ep} was significantly higher in HCC only for the SSM ($p = 0.04$). τ_i was significantly higher in HCC when compared to liver parenchyma ($p = 0.008$). K^{trans} did not show significant differences for either model. Illustrative parametric maps are shown in Fig. 3.

Correlation with histopathology

ART using the TM was significantly higher in moderately differentiated HCCs compared to poorly differentiated HCCs ($p = 0.02$) (Fig. 4a), and borderline higher in HCCs with microvascular invasion compared to those without ($p = 0.05$) (Fig. 4b). All other HCC DCE-MRI parameters showed no significant difference between different tumor
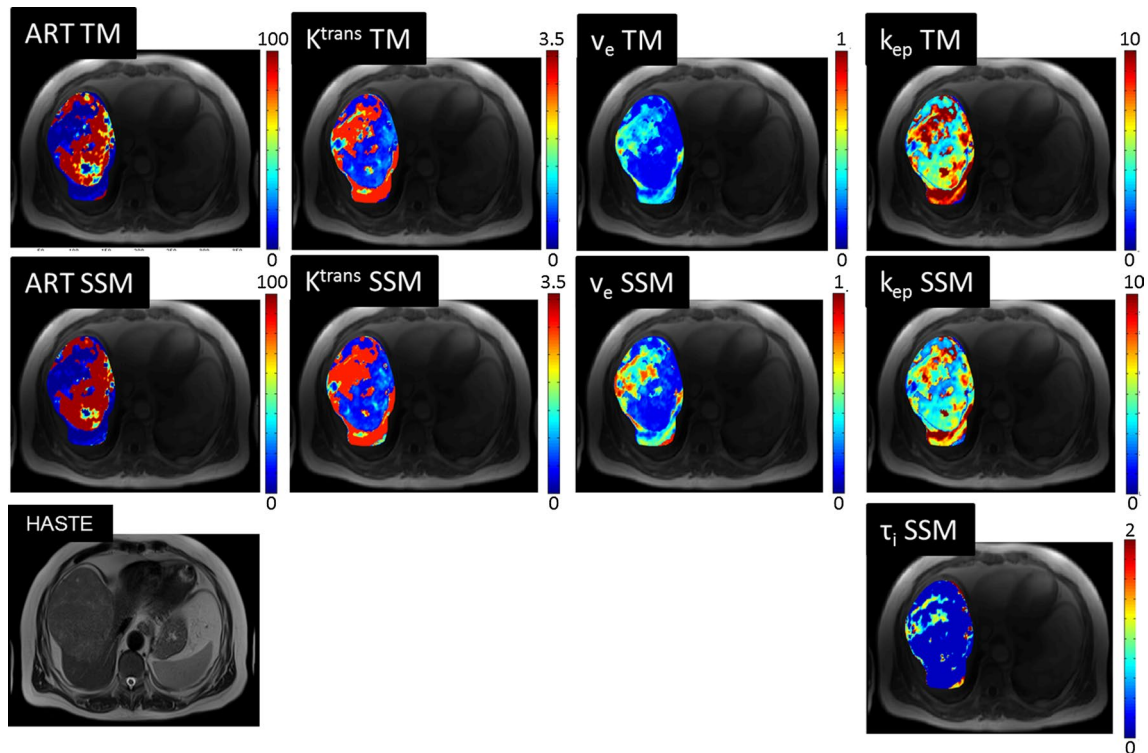
Fig. 3 Axial T2 HASTE, and DCE-MRI parametric maps for same patient as in Fig. 1. Regional differences in the tumor and differences between HCC and background liver parenchyma are visually identified. Estimated perfusion parameters from mean ROI signal intensity for HCC/liver were: for Tofts model, ART 100 %/28 %, K^{trans} 1.1/1.9 min^{-1}, v_e 0.3/0.7, and k_{ep} = 4.2/2.5 min^{-1}; for Shutter-Speed model, ART 100 %/31 %, K^{trans} 1.0/1.8 min^{-1}, v_e 0.3/0.7, k_{ep} 3.8/2.4 min^{-1}, and τ_i 0.1/0.1 s

Fig. 4 *Box plot* distributions of HCC ART measured with Tofts model analysis of DCE-MRI data, in relation to histopathologic parameters in 17 patients with 17 tumors (tumor grade and presence of microvascular invasion)
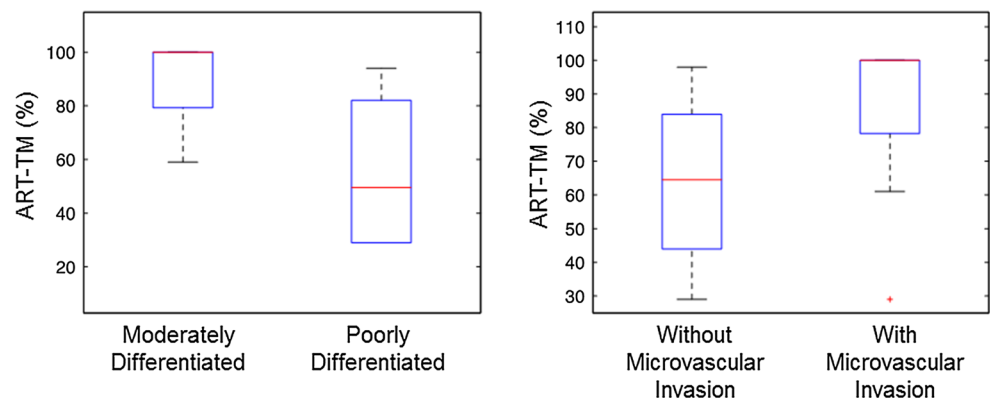
grades and tumors with and without microvascular invasion ($p > 0.07$ and $p > 0.5$, respectively).

Discussion

In this study, we estimated HCC and liver pharmacokinetic parameters and their test–retest reproducibility from DCE-MRI studies using two different pharmacokinetic models: the dual input TM and the dual input SSM. We observed variable parameter reproducibilities for both models when patients underwent test–retest scans on different days. We also found significant differences in certain parameters common to both models, although the observed model differences were smaller than parameter variabilities, suggesting limited clinical impact. Both the TM and the SSM produced parameters significantly different when comparing HCC tumors with liver parenchyma.

In order to reflect more realistic tissue environment, pharmacokinetic models should take into account the

intercompartmental water exchange effects. However, when additional physiological activities are considered, the processing becomes more complex with more parameters estimated [43]. For example, the FXR-allowed SSM version used in this study allows for a non-infinitely fast transcytolemmal exchange, modeled by the mean intracellular water molecule lifetime, τ_i. This parameter has been suggested to reflect cellular metabolic activity, manifest in ATP-driven membrane transport activity in a yeast suspension study [50]. This observation was further validated in a breast DCE-MRI study [51], demonstrating that changes in τ_i are not due to changes in cell sizes but rather changes in energetic metabolism-driven cell membrane water permeability. In our study, we found this parameter to be significantly smaller in the liver parenchyma when compared to HCC lesions, which may be explained by high background metabolic activity in the liver parenchyma [61]. A limitation of this study is the lack of information regarding the metabolic activity of the liver parenchyma and HCC lesions. As the parameter τ_i is linked to energetic metabolism, a study using co-registered FDG-PET/MRI could assist in validating τ_i as an imaging biomarker of metabolic activity.

When using this version of the SSM, we found no significant differences when estimating liver and HCC ART from the acquired DCE-MRI as compared to the TM. It has been suggested that ART can be used to assess response to local regional therapy in HCC [18]. This implies that both the SSM and TM could be used for estimating ART. The SSM returned smaller K^{trans} in the liver and, although not statistically significant, greater K^{trans} in HCC tumors than those of the TM. This is consistent with previous breast [43, 48] and prostate [49] studies showing greater SSM K^{trans} in malignant tumors when compared to TM K^{trans}. Although, the SSM has been used in these breast and prostate studies, it has not been used in liver studies before.

The values of K^{trans} for HCC reported in this study are similar to published values. Zhu et al. [22] found a baseline K^{trans} distribution for HCC between 1.25 and 2.50 min^{-1} and k_{ep} ranging between 1.5 and 3.0 min^{-1} using DCE-MRI for 34 patients enrolled in a phase II study of multitargeted kinase inhibitor sunitinib [62]. Hsu et al. [23] reported baseline K^{trans} between 0.4 and 4.5 min^{-1} in 31 patients with advanced HCC treated with sorafenib plus tegafur/uracil that underwent a DCE-MRI examination. DCE-MRI was used by Hsu et al. [29] who reported smaller baseline values of K^{trans} of approximately 0.3 min^{-1}.

Assessing the reproducibility of estimated perfusion parameters is critical for the purpose of evaluating tumor response to treatment. ART has been recently reported to have a CV of 64.1 % in the liver parenchyma [54] which is similar to the values obtained in the current study. The reproducibility of K^{trans}, v_e and k_{ep} was reported to be 29, 9 and 24 %, respectively, for

different tumor types [63], including renal cell carcinoma, ovarian serous cystadenocarcinoma, peritoneal carcinoma and leiomyosarcoma. In our study, we allowed for a dual input model and therefore, more parameters needed to be estimated. This could have potentially contributed to degrade the reproducibility. While the SSM is more complex than the TM and has an extra modeling parameter, the use of the SSM for data analysis did not result in less reproducible parameters and τ_i was observed to have good reproducibility in the liver.

In this initial study, we found significant differences in the ART of HCC as estimated with the TM when comparing different tumor grades. In poorly differentiated HCCs, ART was decreased due to possibly increased cell proliferation in the tumor center, resulting in an increase of interstitial pressure and the closure of tumor capillaries [64–66]. ART estimated under the TM was higher in lesions with microvascular invasion. This is expected as the invasion is characteristic feature of progressed HCCs with abnormal unpaired arteries [64]. However, these results are preliminary and need to be further confirmed with a larger patient cohort.

One limitation of this study is the relatively small sample size and the fact that only a small subset of HCC lesions had histopathologic results, which reduces power for HCC characterization for many of the DCE-MRI parameters. Another limitation is due to the fact that patients underwent scans of different magnet strengths (1.5 and/or 3.0 T). Ideally, the resulting pharmacokinetic parameters should be independent of imaging conditions as field strength [67], but in practice that might not be the case and different field strengths could be adding variability. Chen et al. [17] identified the choice of contrast agent molecular properties and the temporal resolution of the acquisition as two parameters that influence the quantification of flow and perfusion with DCE-MRI and proposed acquisitions with high enough temporal resolution of 2–5 s to mitigate variability. In this study, we acquired images with an average temporal resolution of 2.3 s and, in addition, only a small set of patients underwent test–retest scans had their scans at different magnet strengths. Nevertheless, the CVs determined in this study agree with those already published in other studies.

Conclusion

In conclusion, our initial data showed differences between liver and HCC perfusion when computed with the TM and SSM pharmacokinetic analyses of DCE-MRI data. The parameters obtained with both models show variable test–retest reproducibilities that depend on the parameter, rendering the model differences in the common parameters insignificant clinical impact. Both models can be used to quantify perfusion differences between HCC and liver parenchyma. However, the additional parameter obtained

with SSM, τ_i, has the potential to provide information about HCC tumor biology, which needs to be better defined in larger study cohorts.

Compliance with ethical standards

References

1. Ferlay J, Shin HR, Bray F, Forman D, Mathers C et al (2010) Estimates of worldwide burden of cancer in 2008: GLOBOCAN 2008. Int J Cancer 127:2893–2917
2. El-Serag HB, Davila JA, Petersen NJ, McGlynn KA (2003) The continuing increase in the incidence of hepatocellular carcinoma in the United States: an update. Ann Intern Med 139:817–823
3. Folkman J (2007) Angiogenesis: an organizing principle for drug discovery? Nat Rev Drug Discov 6:273–286
4. Zhu AX, Duda DG, Sahani DV, Jain RK (2011) HCC and angiogenesis: possible targets and future directions. Nat Rev Clin Oncol 8:292–301
5. Hanahan D, Weinberg RA (2000) The hallmarks of cancer. Cell 100:57–70
6. Hanahan D, Weinberg RA (2011) Hallmarks of cancer: the next generation. Cell 144:646–674
7. Lee JM, Yoon JH, Joo I, Woo HS (2012) Recent Advances in CT and MR Imaging for Evaluation of Hepatocellular Carcinoma. Liver Cancer 1:22–40
8. Earls JP, Theise ND, Weinreb JC, DeCorato DR, Krinsky GA et al (1996) Dysplastic nodules and hepatocellular carcinoma: thin-section MR imaging of explanted cirrhotic livers with pathologic correlation. Radiology 201:207–214
9. Libbrecht L, Bielen D, Verslype C, Vanbeckevoort D, Pirenne J et al (2002) Focal lesions in cirrhotic explant livers: pathological evaluation and accuracy of pretransplantation imaging examinations. Liver Transplant 8:749–761
10. Burrel M, Llovet JM, Ayuso C, Iglesias C, Sala M et al (2003) MRI angiography is superior to helical CT for detection of HCC prior to liver transplantation: an explant correlation. Hepatology 38:1034–1042
11. Taouli B, Losada M, Holland A, Krinsky G (2004) Magnetic resonance imaging of hepatocellular carcinoma. Gastroenterology 127:S144–S152
12. Willatt JM, Hussain HK, Adusumilli S, Marrero JA (2008) MR Imaging of hepatocellular carcinoma in the cirrhotic liver: challenges and controversies. Radiology 247:311–330
13. Guthrie JA (2013) Cirrhosis and focal liver lesions: MRI findings. Imaging 22:68887955
14. Padhani AR (1999) Dynamic contrast-enhanced MRI studies in human tumours. Br J Radiol 72:427–431
15. Padhani AR (2002) Dynamic contrast-enhanced MRI in clinical oncology: current status and future directions. J Magn Reson Imaging 16:407–422
16. Parker GJ, Suckling J, Tanner SF, Padhani AR, Revell PB et al (1997) Probing tumor microvascularity by measurement, analysis and display of contrast agent uptake kinetics. J Magn Reson Imaging 7:564–574
17. Chen B-B, Shih TT-F (2014) DCE-MRI in hepatocellular carcinoma-clinical and therapeutic image biomarker. World J Gastroenterol 20:3125
18. Taouli B, Johnson RS, Hajdu CH, Oei MT, Merad M et al (2013) Hepatocellular carcinoma: perfusion quantification with dynamic contrast-enhanced MRI. Am J Roentgenol 201:795–800
19. Gill AB, Black RT, Bowden DJ, Priest AN, Graves MJ et al (2014) An investigation into the effects of temporal resolution on hepatic dynamic contrast-enhanced MRI in volunteers and in patients with hepatocellular carcinoma. Phys Med Biol 59:3187
20. Orton MR, Miyazaki K, Koh DM, Collins DJ, Hawkes DJ et al (2009) Optimizing functional parameter accuracy for breath-hold DCE-MRI of liver tumours. Phys Med Biol 54:2197–2215
21. Sahani DV, Holalkere NS, Mueller PR, Zhu AX (2007) Advanced hepatocellular carcinoma: CT perfusion of liver and tumor tissue–initial experience. Radiology 243:736–743
22. Zhu AX, Sahani DV, Duda DG, di Tomaso E, Ancukiewicz M et al (2009) Efficacy, safety, and potential biomarkers of sunitinib monotherapy in advanced hepatocellular carcinoma: a phase II study. J Clin Oncol 27:3027–3035
23. Hsu CY, Shen YC, Yu CW, Hsu C, Hu FC et al (2011) Dynamic contrast-enhanced magnetic resonance imaging biomarkers predict survival and response in hepatocellular carcinoma patients treated with sorafenib and metronomic tegafur/uracil. J Hepatol 55:858–865
24. Jarnagin WR, Schwartz LH, Gultekin DH, Gönen M, Haviland D et al (2009) Regional chemotherapy for unresectable primary liver cancer: results of a phase II clinical trial and assessment of DCE-MRI as a biomarker of survival. Ann Oncol 20:1589–1595
25. Yopp AC, Schwartz LH, Kemeny N, Gultekin DH, Gonen M et al (2011) Antiangiogenic therapy for primary liver cancer: correlation of changes in dynamic contrast-enhanced magnetic resonance imaging with tissue hypoxia markers and clinical response. Ann Surg Oncol 18:2192–2199
26. Tofts PS, Kermode AG (1991) Measurement of the blood-brain barrier permeability and leakage space using dynamic MR imaging. 1. Fundamental concepts. Magn Reson Med 17:357–367
27. Tofts PS (1997) Modeling tracer kinetics in dynamic Gd-DTPA MR imaging. J Magn Reson Imaging 7:91–101
28. Tofts PS, Brix G, Buckley DL, Evelhoch JL, Henderson E et al (1999) Estimating kinetic parameters from dynamic contrast-enhanced T(1)-weighted MRI of a diffusable tracer: standardized quantities and symbols. J Magn Reson Imaging 10:223–232
29. Hsu C, Yang TS, Huo TI, Hsieh RK, Yu CW et al (2012) Vandetanib in patients with inoperable hepatocellular carcinoma: a phase II, randomized, double-blind, placebo-controlled study. J Hepatol 56:1097–1103
30. Materne R, Smith AM, Peeters F, Dehoux JP, Keyeux A et al (2002) Assessment of hepatic perfusion parameters with dynamic MRI. Magn Reson Med 47:135–142
31. Annet L, Materne R, Danse E, Jamart J, Horsmans Y et al (2003) Hepatic flow parameters measured with MR imaging and Doppler US: correlations with degree of cirrhosis and portal hypertension. Radiology 229:409–414
32. Hagiwara M, Rusinek H, Lee VS, Losada M, Bannan MA et al (2008) Advanced liver fibrosis: diagnosis with 3D

whole-liver perfusion MR imaging–initial experience. Radiology 246:926–934

33. Patel J, Sigmund EE, Rusinek H, Oei M, Babb JS et al (2010) Diagnosis of cirrhosis with intravoxel incoherent motion diffusion MRI and dynamic contrast-enhanced MRI alone and in combination: preliminary experience. J Magn Reson Imaging 31:589–600

34. Van Beers BE, Materne R, Annet L, Hermoye L, Sempoux C et al (2003) Capillarization of the sinusoids in liver fibrosis: noninvasive assessment with contrast-enhanced MRI in the rabbit. Magn Reson Med 49:692–699

35. Yankeelov TE, Rooney WD, Li X, Springer CS Jr (2003) Variation of the relaxographic "shutter-speed" for transcytolemmal water exchange affects the CR bolus-tracking curve shape. Magn Reson Med 50:1151–1169

36. Li X, Rooney WD, Springer CS Jr (2005) A unified magnetic resonance imaging pharmacokinetic theory: intravascular and extracellular contrast reagents. Magn Reson Med 54:1351–1359

37. Labadie C, Lee JH, Vetek G, Springer CS Jr (1994) Relaxographic imaging. J Magn Reson B 105:99–112

38. Landis CS, Li X, Telang FW, Molina PE, Palyka I et al (1999) Equilibrium transcytolemmal water-exchange kinetics in skeletal muscle in vivo. Magn Reson Med 42:467–478

39. Landis CS, Li X, Telang FW, Coderre JA, Micca PL et al (2000) Determination of the MRI contrast agent concentration time course in vivo following bolus injection: effect of equilibrium transcytolemmal water exchange. Magn Reson Med 44:563–574

40. Springer CS, Rooney WD, Li X (2002) The effects of equilibrium transcytolemmal water exchange on the determination of contrast reagent concentration in vivo. Magn Reson Med 47:422–424

41. Quirk JD, Bretthorst GL, Duong TQ, Snyder AZ, Springer CS et al (2003) Equilibrium water exchange between the intra- and extracellular spaces of mammalian brain. Magn Reson Med 50:493–499

42. Zhou R, Pickup S, Yankeelov TE, Springer CS Jr, Glickson JD (2004) Simultaneous measurement of arterial input function and tumor pharmacokinetics in mice by dynamic contrast enhanced imaging: effects of transcytolemmal water exchange. Magn Reson Med 52:248–257

43. Li X, Huang W, Yankeelov TE, Tudorica A, Rooney WD et al (2005) Shutter-speed analysis of contrast reagent bolus-tracking data: preliminary observations in benign and malignant breast disease. Magn Reson Med 53:724–729

44. Yankeelov TE, Rooney WD, Huang W, Dyke JP, Li X et al (2005) Evidence for shutter-speed variation in CR bolus-tracking studies of human pathology. NMR Biomed 18:173–185

45. Chang E, Li X, Jerosch-Herold M, Priest R, Enestvedt CK et al (2008) The Evaluation of Esophageal Adenocarcinoma Using Dynamic Contrast-Enhanced Magnetic Resonance Imaging. J Gastrointest Surg 12:166–175

46. Li X, Springer CS, Jerosch-Herold M (2009) First-pass dynamic contrast-enhanced MRI with extravasating contrast reagent: evidence for human myocardial capillary recruitment in adenosine-induced hyperemia. NMR Biomed 22:148–157

47. Li X, Huang W, Morris EA, Tudorica LA, Seshan VE et al (2008) Dynamic NMR effects in breast cancer dynamic-contrast-enhanced MRI. Proc Natl Acad Sci 105:17937–17942

48. Huang W, Li X, Morris EA, Tudorica LA, Seshan VE et al (2008) The magnetic resonance shutter speed discriminates vascular properties of malignant and benign breast tumors in vivo. Proc Natl Acad Sci USA 105:17943–17948

49. Li X, Priest RA, Woodward WJ, Tagge IJ, Siddiqui F et al (2013) Feasibility of shutter-speed DCE-MRI for improved prostate cancer detection. Magn Reson Med 69:171–178

50. Zhang Y, Poirier-Quinot M, Springer CS Jr, Balschi JA (2011) Active trans-plasma membrane water cycling in yeast is revealed by NMR. Biophys J 101:2833–2842

51. Springer CS Jr, Li X, Tudorica LA, Oh KY, Roy N et al (2014) Intratumor mapping of intracellular water lifetime: metabolic images of breast cancer? NMR Biomed 27:760–773

52. US Food and Drug Administration (2013) Public health advisory: gadolinium-containing contrast agents for magnetic resonance imaging (MRI) -Omniscan, OptiMARK, Magnevist, ProHance, and MultiHance. Department of Health and Human Services

53. Jajamovich GH, Dyvorne H, Donnerhack C, Taouli B (2014) Quantitative liver MRI combining phase contrast imaging, elastography, and DWI: assessment of reproducibility and postprandial effect at 3.0 T. PLoS ONE 9:e97355

54. Aronhime S, Calcagno C, Jajamovich GH, Dyvorne HA, Robson P et al (2014) DCE-MRI of the liver: effect of linear and non-linear conversions on hepatic perfusion quantification and reproducibility. J Magn Reson Imaging 40:90–98

55. Schabel MC, Parker DL (2008) Uncertainty and bias in contrast concentration measurements using spoiled gradient echo pulse sequences. Phys Med Biol 53:2345

56. Pintaske J, Martirosian P, Graf H, Erb G, Lodemann KP et al (2006) Relaxivity of Gadopentetate Dimeglumine (Magnevist), Gadobutrol (Gadovist), and Gadobenate Dimeglumine (Multi-Hance) in human blood plasma at 0.2, 1.5, and 3 Tesla. Invest Radiol 41:213–221

57. Zhang X, Petersen ET, Ghariq E, De Vis JB, Webb AG et al (2013) In vivo blood T(1) measurements at 1.5 T, 3 T, and 7 T. Magn Reson Med 70:1082–1086

58. Cuenod CA, Balvay D (2013) Perfusion and vascular permeability: basic concepts and measurement in DCE-CT and DCE-MRI. Diagn Interv Imaging 94:1187–1204

59. Huang W, Li X, Chen Y, Li X, Chang MC et al (2014) Variations of dynamic contrast-enhanced magnetic resonance imaging in evaluation of breast cancer therapy response: a multicenter data analysis challenge. Transl Oncol 7:153–166

60. Altman DG (1990) Practical statistics for medical research. CRC Press, Boca Raton

61. Okazumi S, Isono K, Enomoto K, Kikuchi T, Ozaki M et al (1992) Evaluation of liver tumors using fluorine-18-fluorodeoxyglucose PET: characterization of tumor and assessment of effect of treatment. J Nucl Med 33:333–339

62. Papaetis GS, Syrigos KN (2009) Sunitinib: a multitargeted receptor tyrosine kinase inhibitor in the era of molecular cancer therapies. BioDrugs 23:377–389

63. Galbraith SM, Lodge MA, Taylor NJ, Rustin GJ, Bentzen S et al (2002) Reproducibility of dynamic contrast-enhanced MRI in human muscle and tumours: comparison of quantitative and semi-quantitative analysis. NMR Biomed 15:132–142

64. Choi JY, Lee JM, Sirlin CB (2014) CT and MR imaging diagnosis and staging of hepatocellular carcinoma: part I. Development, growth, and spread: key pathologic and imaging aspects. Radiology 272:635–654

65. Asayama Y, Yoshimitsu K, Irie H, Nishihara Y, Aishima S et al (2007) Poorly versus moderately differentiated hepatocellular carcinoma: vascularity assessment by computed tomographic hepatic angiography in correlation with histologically counted number of unpaired arteries. J Comput Assist Tomogr 31:188–192

66. El-Assal ON, Yamanoi A, Soda Y, Yamaguchi M, Igarashi M et al (1998) Clinical significance of microvessel density and vascular endothelial growth factor expression in hepatocellular carcinoma and surrounding liver: possible involvement of vascular endothelial growth factor in the angiogenesis of cirrhotic liver. Hepatology 27:1554–1562

67. Tofts PS (2010) T1-weighted DCE imaging concepts: modelling, acquisition and analysis. MAGNETOM Flash: 30–39